JOURNAL OF GEOPHYSICAL RESEARCH, VOL. 113, D17211, doi:10.1029/2007JD009648, 2008

Composition-resolved size distributions of volcanic aerosols in the Mt. Etna plumes

R. S. Martin,[1] T. A. Mather,[2] D. M. Pyle,[2] M. Power,[3,4] A. G. Allen,[5] A. Aiuppa,[6,7] C. J. Horwell,[8] and E. P. W. Ward[9]

Received 28 November 2007; revised 4 April 2008; accepted 16 April 2008; published 12 September 2008.

[1] Particle size distributions for soluble and insoluble species in Mt. Etna's summit plumes were measured across an extended size range (10 nm < d < 100 μm) using a combination of techniques. Automated scanning electron microscopy (QEMSCAN) was used to chemically analyze many thousands of insoluble particles (collected on pumped filters) allowing the relationships between particle size, shape, and composition to be investigated. The size distribution of fine silicate particles (d < 10 μm) was found to be lognormal, consistent with formation by bursting of gas bubbles at the surface of the magma. The compositions of fine silicate particles were found to vary between magmatic and nearly pure silica; this is consistent with depletion of metal ions by reactions in the acidic environment of the gas plume and vent. Measurements of the size, shape and composition of fine silicate particles may potentially offer insights into preemission, synemission, and postemission processes. The mass flux of fine silicate particles from Mt. Etna released during noneruptive volcanic degassing in 2004 and 2005 was estimated to be ~7000 kg d^{-1}. Analysis of particles in the range 0.1 < d/μm < 100 by ion chromatography shows that there are persistent differences in the size distributions of sulfate aerosols between the two main summit plumes. Analysis of particles in the range 0.01 μm < d < 0.1 μm by scanning transmission electron microscopy (STEM) shows that there are significant levels of nanoparticles in the Mt. Etna plumes although their compositions remain uncertain.

Citation: Martin, R. S., T. A. Mather, D. M. Pyle, M. Power, A. G. Allen, A. Aiuppa, C. J. Horwell, and E. P. W. Ward (2008), Composition-resolved size distributions of volcanic aerosols in the Mt. Etna plumes, *J. Geophys. Res.*, *113*, D17211, doi:10.1029/2007JD009648.

1. Introduction

[2] Mt. Etna (37.734°N, 15.004°E) is Europe's most active volcano, well known as a prodigious source of reactive gases and trace metals to the regional troposphere [e.g., *Allard et al.*, 1991; *Caltabiano et al.*, 1994; *Bagnato et al.*, 2007]. Mt. Etna has been in a heightened state of activity since 1998 [*Allard et al.*, 2006] and is responsible for a persistent gas and aerosol plume which is sustained by degassing from the four summit craters, at an elevation of around 3300 m. This sustained degassing makes Mt. Etna an ideal location to study the interactions between volcanic gas, aerosol and the ambient atmosphere [e.g., *Aiuppa et al.*, 2003, 2005a, 2005b], in particular since it is possible to collect aerosol and gas samples from close proximity to the active vents.

[3] Previous studies of the aerosols from Mt. Etna have taken three distinct but complementary approaches: plume spectrometry [*Watson and Oppenheimer*, 2000, 2001], chemical analysis of bulk plume particle samples [e.g., *Gauthier and Le Cloarec*, 1998; *Aiuppa et al.*, 2003, 2006] and particle microscopy [e.g., *Varekamp et al.*, 1986; *Toutain et al.*, 1995]. These techniques are able to offer information on particle size distributions, bulk particle chemistry and single particle morphology but none of these previous studies have been able to examine particle-by-particle correlations among these properties (i.e., how the size, shape and composition of particles are dependent on one another). Recent advances in the understanding of the radiative, chemical and health properties of volcanic aerosols have shown that a unified understanding of the chemical and morphological character of aerosols is vital for

[1]Department of Earth Sciences, University of Cambridge, Cambridge, UK.
[2]Department of Earth Sciences, University of Oxford, Oxford, UK.
[3]Intellection U. K. Limited, Conwy, UK.
[4]Camborne School of Mines, University of Exeter, Cornwall, UK.
[5]Analytical Chemistry Department, Chemistry Institute, Sao Paulo State University, Araraquara, Brazil.
[6]Dipartimento di Chimica e Fisica della Terra e Applicazioni alle Georisorse e ai Rischi Naturali, Università degli Studi di Palermo, Palermo, Italy.
[7]Also at Sezione di Palermo, Istituto Nazionale di Geofisica e Vulcanologia, Palermo, Italy.
[8]Institute of Hazard and Risk Research and Department of Earth Sciences, Durham University, Durham, UK.
[9]Department of Materials Science and Metallurgy, University of Cambridge, Cambridge, UK.

0148-0227/08/2007JD009648$09.00

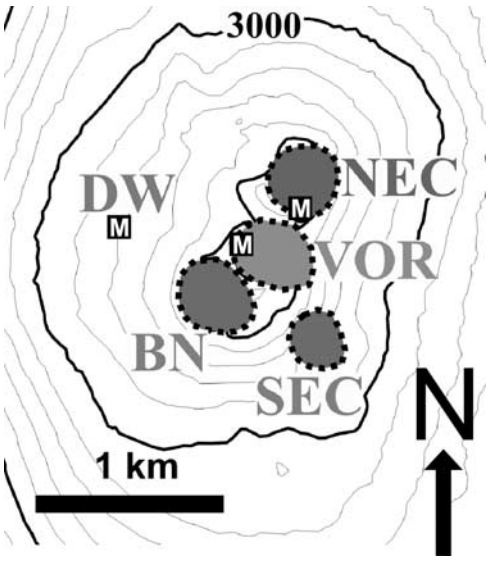

Figure 1a. The summit of Mt. Etna (37.734°N, 15.004°E). Contours are given for 50 m increments in altitude. North East Crater (NEC), Voragine (VOR), Bocca Nuova (BN), South East Crater (SEC), and the downwind site (DW) are labeled. Sampling locations are labeled as "M." For further information on Mt. Etna, see http://www.vulcanoetna.it/en.php.

assessing the role and impact of these species [*Mather et al.*, 2003b; *Horwell and Baxter*, 2006].

[4] In this study, particles were sampled from the plumes of Mt. Etna in 2004–2005 using filter packs and analyzed using automated scanning electron microscopy (QEMSCAN) [*Pirrie et al.*, 2004]. QEMSCAN allows the relationships between particle size, shape and composition to be investigated by analyzing thousands of individual particles. In addition, micro-orifice uniform deposit impactor (MOUDI) samples were collected and analyzed using ion chromatography (IC) to investigate the size distribution of soluble particles. Filter pack samples were also analyzed using ion chromatography to measure the total concentrations of soluble ions in the gas and particle phases. Finally, samples were also collected using a thermophoretic precipitator and analyzed using scanning transmission electron microscopy (STEM) to calculate the size distribution of nanoparticles ($0.01 < d/\mu m < 0.1$) in Mt. Etna's plumes. The combination of these techniques allows characterization of the chemical and physical characteristics of Mt. Etna's particles over an unprecedented size range.

2. Sample Locations

[5] Samples were collected from the crater rims of Mt. Etna's two main degassing vents (at the time of sampling): North-East Crater (NEC) and Voragine (VOR) (Figure 1a). Cross sections for the two craters are shown in Figure 1b.

[6] The shortest time between emission and collection (i.e., the plume age) of gas and particles was estimated to be ~30 s at both craters [*Aiuppa et al.*, 2005a]. However, swirling was observed at the larger NEC (as shown in Figure 1b) at the time of sampling and so plume arriving at the crater rim may be a mixture of younger and more aged components. Furthermore, small magma spattering explosions were audible at the NEC crater rim, suggesting the plume might have a higher silicate ash content than the Voragine plume. The plume is typically blown to the southeast; however, the downwind samples (DW) were collected on a day when the plume was blown to the west. Observations made at the time of sampling suggest the plume sampled downwind was a mixture of NEC and Voragine plumes with a plume age on the order of a few minutes. An additional MOUDI sample was made directly above a degassing fracture on a fresh lava flow at Piano Provenzana (37.798°N, 15.038°E, altitude ~ 1800 m) in November 2002. Background (BG) samples were taken close to Piano Provenzana in 2005; the sampling location in 2005 was distal from any identified volcanic or anthropogenic emission sources (e.g., heavy traffic or industry). Table 1 summarizes the details for each sample taken in this study.

3. Methodology

3.1. Filter Packs

[7] Filter packs (FP) consist of four filters housed in a multiple-stage cartridge (47 mm in diameter), pumped at rates of 8–24 L min^{-1}. The plume was pumped through a particle filter (Millipore, 47 mm, AAWP, pore size 0.8 μm), followed by three identical acid gas filters (Whatman 41 ashless circles impregnated with 10% $NaHCO_3$ and 10% glycerol in 1:1 methanol/distilled deionized water). This type of acid gas filter converts acidic gases (e.g., SO_2 and HCl,) to their weakly basic counter-anions (e.g., SO_4^{2-} and Cl^-) with an efficiency of 80–90% (T. A. Mather, unpublished data, 2003) under sampling conditions comparable those of the Mt. Etna field campaign (e.g., sampling durations of <3 h at the crater rim of Masaya volcano, Nicaragua). Sampling times ranged from ~10 min to ~2 h at the summit sites (NEC, VOR, DW) and ~2 h at the background site; in total 11 summit filter pack samples and 1 background filter pack sample were taken (Table 1). After collection, filters were triple-sealed in individual

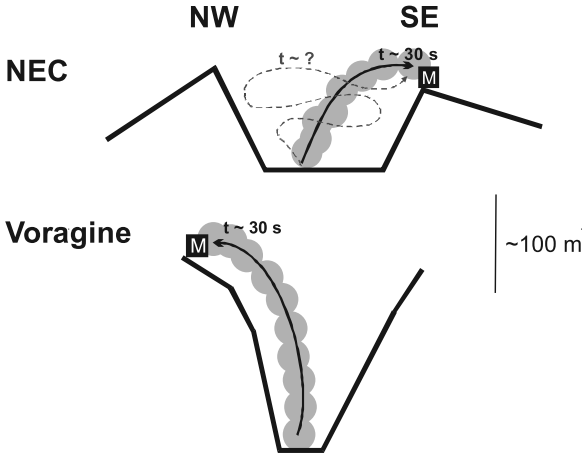

Figure 1b. Cross sections of North East Crater (NEC) and Voragine (VOR). The plume age in both cases was at least 30 s. Plume arriving at the NEC sampling location may also contain a more aged component.

Table 1. List of Samples[a]

Date	Sample	Location	Local Time	Duration (h:min)	P/hPa	T/°C	RH%	Flow/L min^{-1}
27 August 2005	FP01:QM01	NEC	1128–1148	00:20	688	22–24	31–28	12–16
27 August 2005	FP02	NEC	1151–1231	00:40	688	18–19	31–27	16
27 August 2005	MD01	NEC	1057–1357	03:00	688	25–13	37–38	8–9
28 August 2005	MD02	VOR	1100–1430	03:30	692	8–11	34–40	8
28 August 2005	FP03:QM02	VOR	1113–1123	00:10	692	10	36–24	14–16
28 August 2005	FP04	VOR	1148–1208	00:20	692	10–12	46–56	19
29 August 2005	MD03	NEC	1136–1343	02:07	685	9–6	35–68	8
29 August 2005	FP05	NEC	1158–1218	00:20	685	9–7	31–35	24
30 August 2005	MD04	BG	1037–1702	06:25	968	25–23	71–77	10–8
30 August 2005	FP06	DW	1209–1256	00:47	704	7–6	46–67	19–20
30 August 2005	FP07	DW	1300–1419	01:19	704	7–4	69–80	19–8
31 August 2005	FP08	BG	1340–1538	01:58	821	16–17	63–59	20
2 September 2005	MD05	VOR	0950–1140	01:50	690	9–13	72–64	6–4
2 September 2005	FP09	VOR	0959–1158	01:59	690	10	72–78	16–6
2 September 2005	FP10	VOR	1144–1239	00:55	692	12–13	61–67	16
3 September 2005	FP11	NEC	1030–1130	01:00	689	16–20	37–42	19–13
3 September 2005	FP12	NEC	1038–1200	01:22	689	15–17	40–30	18
30 July 2004	QM03	VOR	1218–1246	00:28	692	16–13	38–55	16–15
27 August 2005	TP01	NEC	1211–1311	00:60	688	17–22	30–33	1
28 August 2005	TP02	VOR	1102–1157	00:55	692	9	35–50	1
1 November 2002	FL01	PP	1204–1304	00:60	-	-	-	10

[a]Abbreviations: MD, MOUDI impactor sample; FP, filter pack sample for IC analysis; QM, filter pack sample for automated scanning electron microscopy (QEMSCAN) analysis. Sampling locations (see Figure 1a): NEC, North East Crater; VOR, Voragine crater; BG, background; DW, downwind; PP, Piano Provenzana 2002 lava flow. *P*, *T*, and RH% denote pressure, temperature, and relative humidity measured at the time of sampling. Ranges are given to indicate sampling conditions at the start and end of each run.

plastic bags and stored in a freezer to limit the risk of further reaction.

3.2. Micro-Orifice Uniform Deposition Impactor

[8] A micro-orifice uniform deposition impactor (MOUDI, MSP Corporation) was used to achieve size-selective impaction of particles onto 12 stages. The standard cutoff diameters (d_{50}) are defined by the aerodynamic diameter (d_a) at which 50% of the particles will be impacted onto the stage. However, as the cutoff characteristics of the instrument are sharp, d_{50} is approximately equivalent to the minimum diameter of the particle which will be impacted onto each stage. The standard cutoff diameters (d_{50}) for the instrument were 18 μm, 9.9 μm, 6.2 μm, 3.1 μm, 1.8 μm, 1 μm, 0.55 μm, 0.325 μm, 0.175 μm, 0.099 μm and 0.054 μm for a flow rate of 30 L min^{-1}. These aerodynamic diameters are generally larger than the equivalent diameters (d) measured by QEMSCAN (3.5) or STEM (3.6).

[9] In this study, PTFE filters were used in the top and numbered (1–10) stages with a quartz filter used in the backup stage. Air was drawn through the MOUDI at a flow rate of 4–10 L min^{-1} by a pump powered by a 12V car battery. The flow rates achieved were less than standard conditions (30 L min^{-1}) for the MOUDI. The real cutoff diameters (d_{50}*) were calculated from standard cutoff diameters using the conversion formula predicted by Stokesian theory, equation (1) [*Hinds*, 1999; MSP Corporation, personal communication, 2003].

$$d_{50}^{*} = d_{50}\sqrt{\frac{30}{F}} \quad (1)$$

where F is the measured flow rate in L min^{-1}. Although the theory is sound, it remains untested whether this simple relationship can be applied at low flow rates. This issue has been encountered previously in MOUDI studies of volcanic plumes [*Mather et al.*, 2003a, 2004b]. However, while the cutoff diameters (d_{50}*) should perhaps be treated as qualitative, the shape of the particle size distribution is unlikely to be affected significantly by operating at a low flow rate. A potentially greater concern is the variation in flow rate over a single run as this may lead to broadening of the calculated size distribution. The maximum variation in flow rate observed (MD05) leads to variation in d_{50}* of ~20%; this corresponds to a shift of ~0.08 log(d_a) units over the course of the run and so the effect on the shape of the calculated size distributions is small. Sample collection times ranged from ~2 h to ~4 h at the summit sites (NEC, VOR) and ~6 h at the background site; in total 4 summit MOUDI samples and 1 background MOUDI sample were taken. After collection, filters were triple sealed in individual bags and stored in a freezer to prevent further reaction.

3.3. Thermal Precipitation

[10] Samples were collected from the North-East Crater and Voragine plumes using a thermal precipitator (TP) based on the design of *Maynard* [1995]. The instrument produces a thermal gradient between two plates (ΔT = 100°C, $\nabla T = 10^6$ °C m^{-1}) causing deflection of the particles in a direction perpendicular to the flow and resulting in deposition onto a 3 mm diameter carbon-coated Ni grid (Agar Scientific, United Kingdom). The deposition efficiency is independent of particle size between 4 nm and ~40 nm and becomes less efficient at higher particle diameters. The sampling flow rate was ~1 L min^{-1} for ~1 h in both runs. After collection, samples were placed in a grid box and stored in a freezer to prevent further reaction.

3.4. Ion Chromatography

3.4.1. IC Analysis of FP Samples

[11] All filters (i.e., particle and acid gas) were cut into thirds in a laminar flow clean hood; two sectors from each

Table 2. Relative Uncertainty on the Measurement of Extract Concentration at 1 ppm and the Concentration of Ions in the Plume[a]

	F^-	Cl^-	Br^-	NO_3^-	SO_4^{2-}	Na^+	NH_4^+	K^+	Ca^{2+}
$\delta x/x$	0.11	0.19	0.15	0.10	0.11	0.05	0.23	0.06	0.23
δ[X]/[X]	0.16	0.24	0.20	0.15	0.16	0.10	0.28	0.11	0.28

[a]Extract concentration, x; concentration of Ions in the plume, $[X]_{tot}$ (equation (2)) and [X] (equation (3)).

filter were retained for future studies (the distribution of material on the filter is assumed to be homogeneous). The remaining sector from each of the three acid gas filters were combined and placed together in a polypropylene vial and extracted with 20 ml distilled deionized water. The sector from the particle filter was extracted separately using the same method. Extraction was aided by mechanical agitation for 12 h. All extracts were diluted a further 10 times with distilled deionized water and one drop of 30% H_2O_2 was added to the acid gas filter extracts immediately prior to analysis to oxidize SO_3^{2-} to SO_4^{2-}. The diluted extracts were analyzed by Dionex ion chromatography (IC) using gradient analysis with distilled deionized water and 0.1 M NaOH (for anions) or 30 mN H_2SO_4 (for cations) as eluents as in the work of *Mather et al.* [2004a, 2004b] with additional quantification of Br^-. This technique allows for quantification of F^-, Cl^-, Br^-, NO_3^-, SO_4^{2-}, Na^+, NH_4^+, K^+ and Ca^{2+} species within the extracts (ppm by mass).

[12] The anion and cation IC instruments were calibrated once daily with standard solutions of concentrations of ions ranging from 0.01–50 ppm. All calibrations were made using a point-to-point fit; however, in most cases, the fitting approximated to linear over the entire concentration range. For Ca^{2+} and K^+ the fitting deviated from linear at 0.01 ppm suggesting that the lower end of the calibration scale (i.e., 0.01 ppm) approached the limit of detection for these ions. No drift was observed in the 3 days over which the analyses were performed. Uncertainties are calculated as one standard deviation of the measured return on the concentrations of standard solutions of 1 ppm interspersed throughout the run (n = 3 per day) (Table 2).

[13] Analysis of extracts from blank particle (n = 3) and acid gas (n = 3) filters showed that contamination of the extracts was less than 0.01 ppm for all ions. The contaminations of blanks were outside of the calibration scale (i.e., <0.01 ppm) so it was not necessary to adjust the sample results.

3.4.2. IC Analysis of MOUDI Samples

[14] All filters were cut into sixths in a laminar flow clean hood. Two nonadjacent sectors were extracted with 1 ml propan-2-ol (to "wet" the hydrophobic PTFE), followed by 19 ml distilled deionized water. The extracts were then analyzed without further dilution using ion chromatography (as described in section 3.4.1) to determine the concentrations of ions (F^-, Cl^-, Br^-, NO_3^-, SO_4^{2-}, Na^+, NH_4^+, K^+, and Ca^{2+}) in the extracts. Analysis of extracts from blank PTFE (n = 3) and quartz substrates (n = 3) showed that the contaminations of blanks were outside of the calibration scale (i.e., <0.01 ppm) so it was not necessary to adjust the sample results. Sample FL01 was analyzed in an earlier session on the IC instrument; measurement uncertainties in this earlier session were comparable to those shown in Table 2.

3.5. Automated Scanning Electron Microscopy

[15] Particle filters (QM01, QM02, and QM03) were analyzed using automated scanning electron microscopy (QEMSCAN) [*Pirrie et al.*, 2004] to determine the size, shape and composition of ~5000 particles on each filter. To prepare the samples for analysis, a 25 mm diameter circle was cut from each particle filter (in order to fit the mount) and coated with carbon to a thickness of 25 Å. Following preparation, the samples were loaded into the QEMSCAN instrument and the analysis was started. Particles with diameters between 0.2 μm and 10 μm were automatically located (and imaged) using the contrast in the backscattered electron signal between particles and the filter. Subsequently, four energy dispersive X-ray spectrometers were scanned across each located particle with a beam stepping interval (i.e., spacing between acquisition points) of 0.2 μm, an accelerating voltage of 25 keV and a beam current of 5 nA. Interactions between the beam and the sample were modeled using a Monte Carlo simulation; this simulation allows the collection of spectra to be performed at a higher resolution than the beam width (~2 μm). The spectra were then compared with spectra held in a look-up table allowing an assignment to be made of a chemical composition at each acquisition point. The look-up table contains entries for silicates, sulfate and sulfide species of variable compositions (Table 3); the assignment makes no distinction between mineral species and amorphous grains of similar composition. This procedure allows a compositional map of the particle to be generated. These maps were output as an index file where each particle is represented by a scaled image (scale: 0.2 μm pixel^{-1}) with pixel coloring denoting the assigned composition (Figure 2). Image analysis software (ImageJ; see http://rsb.info.nih.gov/ij) [*Abramoff et al.*, 2004] was used to fit an equivalent ellipse (with equivalent area, centroid, and orientation) to each particle in the index file. The major (a) and minor (b) axes of the ellipse were used to calculate an equivalent particle diam-

Table 3. QEMSCAN Look-Up Table[a]

Composition	Type
Si-O	Silicate (metal-poor)
K-Al-Si-O	Silicate (metal-rich)
Ca-Na-Al-Si-O	Silicate (metal-rich)
Fe-Al-Si-O	Silicate (metal-rich)
Ca-Fe-Si-O	Silicate (metal-rich)
Ca-Al-Si-O	Silicate (metal-rich)
Mg-Fe-Al-Si-O	Silicate (metal-rich)
Mg-Fe-Si-O	Silicate (metal-rich)
Ca-S-O	Sulfate
Al-S-O	Sulfate
Fe-S-O	Sulfate
Fe-Al-S-O	Sulfate
K-S-O	Sulfate
Na-S-O	Sulfate
Na-K-S-O	Sulfate
Na-Mg-Fe-S-O	Sulfate
S	Sulfur/Sulfide
Fe-S	Sulfur/Sulfide

[a]The assignment does not distinguish between mineral and amorphous species of similar composition.

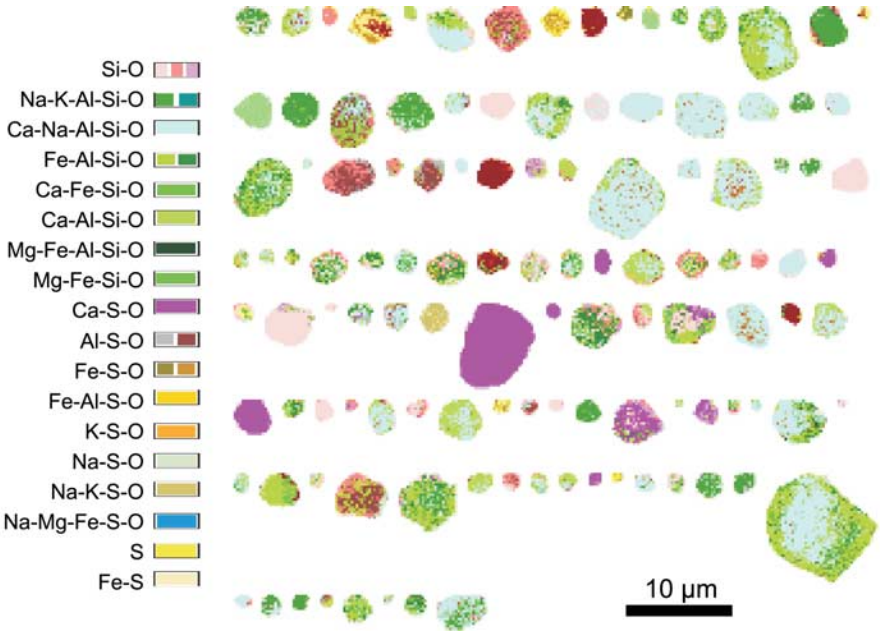

Figure 2. An excerpt from the automated scanning electron microscopy (QEMSCAN) index file (QM02) with color key. The excerpt is only a small subset of the entire index file and so may not be fully representative of the sample.

eter from $d = \sqrt{(ab)}$; these results were stored in a spreadsheet to facilitate further processing. Each entry (i.e., particle) in this spreadsheet was further annotated with an assignment (i.e., silicates, sulfates, or sulfide) by inspection of the compositional map of the particle.

[16] Results were also output directly by the QEMSCAN software as an additional spreadsheet giving the weight percent (wt%) of each composition in the look-up table (Table 3) at 1 μm particle size intervals (i.e., for 0–1 μm, 1–2 μm etc.). These results are semiquantitative because the weight percent of each composition was calculated from the compositional assignments (rather than the original EDX signals) using an approximate stoichiometry for each composition. This limitation reflects the design of the instrument which is optimized for rapid compositional identification, rather than detailed compositional analysis. The silicate compositions were grouped into "metal-rich" (all identified phases of the form M-Si-O) and "metal-poor" (Si-O). An assignment of the latter implies that the intensity of EDX signals attributable to metals were small, hence metal-poor is approximately synonymous with nearly pure silica. We define the parameter Z to equal (Si-O wt%)/(Si-O wt% + M-Si-O wt%). The limits of $Z = 0$ and $Z = 1$ denote the metal-rich and metal-poor end-members, respectively.

3.6. Analysis of TP Samples With Scanning Transmission Electron Microscopy

[17] Images of particle fields were acquired using a Tecnai F20 microscope operated at 200 keV by scanning a narrow probe of electrons across the sample and recording the intensity of the transmitted electrons scattered to high angles using a high-angle annular dark field (HAADF) detector. The near-vacuum operational pressure of the instrument causes the evaporation of liquid droplets. Hence, the nanoparticles imaged are either deposited as solids, or as liquids that evaporate during storage or analysis to form precipitates.

[18] Particle fields (Figure 3) of area $\sim$4 μm^2 were selected randomly and imaged. Scale bars are shown for 1 μm, 100 nm and 10 nm. Each gray-scale image was then processed with image analysis software (ImageJ) to subtract the background and enhance contrast. This processing was followed by thresholding to produce an image of particles (black) on a white background (Figure 3). Threshold limits were chosen using the onset of inclusion of background shown by a marked increase in the number of dark pixels. Image analysis was then used to generate a spreadsheet containing shape and size data for each particle (see section 3.5). To allow for uneven particle deposition on the grid, several particle fields were analyzed from each sample. Particles with $d < 10$ nm were not considered, since genuine nanoparticles, particles formed by splashing upon impaction from large droplets and errant pixels (an artifact of image processing) could not be reliably distinguished below this scale. Also, particles with $d > 100$ nm were not considered because collection is unlikely to be quantitative for these particles [*Maynard*, 1995]. Particle fields were found to have loadings of between 25 and 125 particles μm^{-2} for $10 < d/\text{nm} < 100$.

3.7. Data Analysis

3.7.1. Concentration of Ions in the Plume

[19] The concentration of ions in the plume from FP results, $[X]_{tot}$ (μmol m^{-3}), were calculated with equation (2) (measurement uncertainties in Table 2)

$$[X]_{tot} = \frac{x \lambda m_{ext}}{A M_r V_p} \quad (2)$$

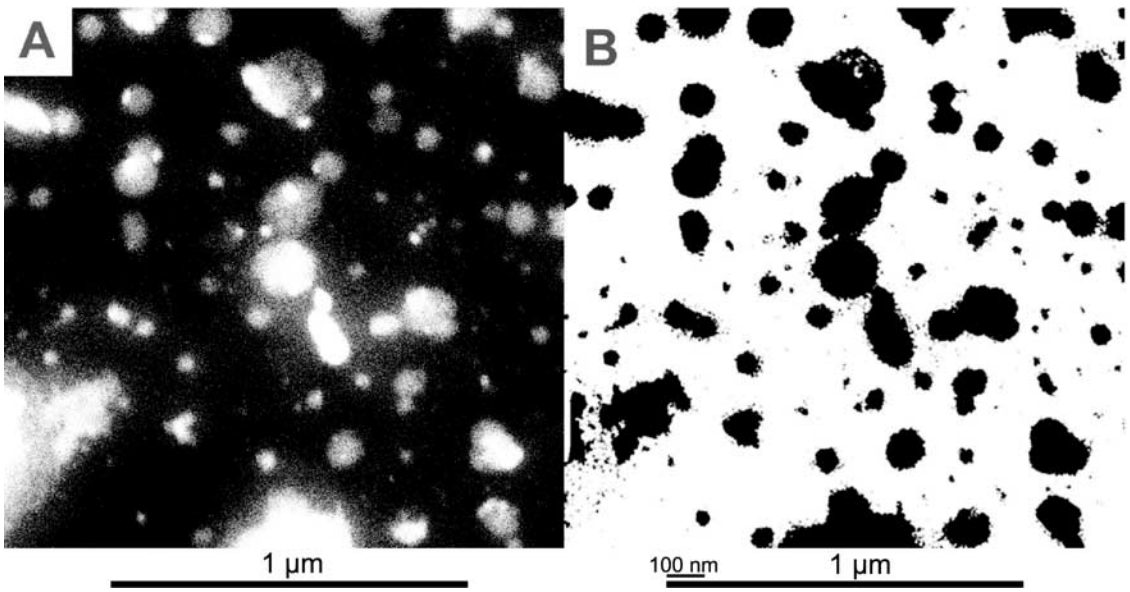

Figure 3. A particle field imaged using STEM-HAADF. (a) The unprocessed image of the particle field. (b) The processed black and white image.

where x (ppm) is the measured concentration of the ion in the extract, λ is the dilution factor ($\lambda = 10$ in this case), m_{ext} (g) is the mass of extract, M_r (g mol^{-1}) is the molar mass of the ion, V_p (m^3) is the volume of plume sampled and A is the fraction of filter analyzed (A = 1/3 in this case). An additional 5% uncertainty on $[X]_{tot}$ is allowed (Table 2) to take into account uncertainty on the measurement of flow rates.

3.7.2. Concentration Density Distribution

[20] MOUDI-IC results were used to calculate the concentration density distribution, [X] (μmol m^{-3}), equation (3). [X] is defined such that integration in $\log(d_a)$ between two limits gives the amount of an ion in particles with aerodynamic diameters between these limits per cubic meter of plume.

$$[X] = \frac{x\lambda m_{ext}}{AM_r V_p} \frac{1}{d\log(d_a)} \tag{3}$$

[21] Parameters are defined as in (2). The term, $d\log(d_a)$ is a normalization factor for the class-width defined by the difference between the upper and lower cutoff diameter in $\log(d_a)$ space (i.e., the size range over which particles are impacted on each stage). For all the numbered stages, $d\log(d_a) \sim \log 2$. [X] is plotted at the geometric midpoint of the upper and lower cutoff diameter, e.g., for two adjacent stages with d_{50}* = 3.4 μm and d_{50}* = 1.9 μm, particles in the range $1.9 < d_a/\mu m < 3.4$ will be impacted on the second stage so we plot [X] at 2.5 μm. For the top and bottom stages, we use $d\log(d_a) \sim \log 2$; the true class-width will be slightly larger.

3.7.3. Number Density Distribution

[22] In this study, particle size distributions are described by the number density distribution, $N(d)$ (m^{-3}), as given in equation (4). $N(d)$ is defined such that integration in $\log(d)$ between two limits gives the number of particles with diameters between these limits per cubic meter of plume.

$$N(d) = \frac{dN}{d\log d} \tag{4}$$

[23] The techniques used in this study do not allow direct measurement of $N(d)$ and conversions must be applied to calculate $N(d)$ from the native format of the data. For the retrieval of $N(d)$ from image analysis data (i.e., lists of particle sizes), we define the number density distribution of imaged particles, $n(d)$ (unitless) as given by equation (5); $n(d)$ can be calculated directly from the spreadsheet output of the image analysis software.

$$n(d) = \frac{dn}{d\log d} \tag{5}$$

[24] For QEMSCAN data, $N(d)$ can be calculated from $n(d)$ by dividing by the area fraction of filter analyzed, A (unitless, recorded by QEMSCAN) and the volume of plume sampled, V_p (m^3; determined from flow rate measurements) (equation (6a)). For thermal precipitator data, $N(d)$ is proportional to the sampling time and $n(d)$. To calculate $N(d)$, we must divide $n(d)$ by the area of grid analyzed, B (m^2), the sampling duration, t (s) and the theoretical deposition flux of the instrument (D = 0.03 m s^{-1}) [*Maynard*, 1995].

$$N(d) = \frac{1}{AV_p} n(d) \tag{6a}$$

$$N(d) = \frac{1}{BDt} n(d) \tag{6b}$$

Table 4a. Analysis of FP samples: Particle Filters[a]

Sample	Location	F^-	Cl^-	NO_3^-	SO_4^{2-}	Na^+	NH_4^+	K^+	Ca^{2+}
FP01P	NEC	4.6	2.5	1.3	49	12	0.93	3.3	0.22
FP02P	NEC	2.1	1	0.6	19	25	0.47	1.4	0.16
FP03P	VOR	1.4	2.4	2.8	22	77	1.7	2.6	0.56
FP04P	VOR	4.7	2.9	1.6	22	7.8	0.67	17	0.24
FP05P	NEC	5	1.8	0.17	59	17	0.87	1.3	0.14
FP06P	DW	12	15	3.7	36	5	0.62	0.99	0.084
FP07P	DW	4.5	3.3	1.9	8	1.7	0.27	0.44	0.046
FP08P	BG	0.11	0.3	1.1	0.72	1.5	1.9	0.15	0.027
FP09P	VOR	3.3	0.5	0.15	16	7.3	1.9	0.54	0.074
FP10P	VOR	5.6	0.48	0.35	39	2.3	3.9	0.8	0.051
FP11P	NEC	0.89	4.1	0.87	17	7.8	0.32	1.6	0.51
FP12P	NEC	0.47	0.58	0.015	13	3.9	0.25	0.83	0.029
Mean	NEC (n = 5)	2.6	2	0.6	32	13	0.57	1.7	0.21
Mean	VOR (n = 4)	3.7	1.6	1.2	25	24	2	5.2	0.23
Mean	DW (n = 2)	8.3	9.2	2.8	22	3.3	0.44	0.71	0.065

[a]The concentrations of ions in the plume, $[X]_{tot}$, are given in units of μmol m^{-3}. Measurement uncertainties are given in Table 2.

3.7.4. Volume Density Distribution

[25] The volume density distribution, $V(d)$ (μm^3 m^{-3}), can be estimated from $N(d)$ with equation (7).

$$V(d) = \frac{\pi}{6} d^3 N(d) \tag{7}$$

[26] This transformation assumes all particles can be described by an equivalent sphere defined with diameter d equal to $\sqrt{(ab)}$. In the absence of any information on the depth axis (c), this assumption is necessary.

3.7.5. Elongation

[27] Elongation, E, was used to define particle shape and can take values from zero ($a = b$; spherical particles) to 1. The parameters a and b are the major and minor axes of the ellipse fitted to each particle by image analysis software (equation (8)).

$$E = 1 - \frac{b^2}{a^2} \tag{8}$$

4. Results and Discussion

4.1. FP-IC

[28] FP samples (i.e., particle and acid gas filters) were analyzed to measure the concentration (ppm) of F^-, Cl^-, Br^-, NO_3^-, SO_4^{2-}, Na^+, NH_4^+, K^+ and Ca^{2+} in the extract solutions. These results were used to derive $[X]_{tot}$ using (2); results for particle filters and acid gas filters are shown in Tables 4a and 4b, respectively. The concentrations of particulate Br^- measured in the extracts were typically <0.01 ppm (i.e., the bottom of the calibration scale) so results are not reported. $[X]_{tot}$ is a measure of the time-averaged concentration of each species at the sampling site and so depends on the proportion of time the sampling site was within the plume. For the purposes of flux estimation, $[X]_{tot}/SO_2$ was calculated for each sample with results averaged to give mean $[X]_{tot}/SO_2$ for each location (Table 5).

[29] Increased HCl/SO_2 and HF/SO_2 for NEC relative to Voragine are consistent with the findings of *Aiuppa et al.* [2005a], who report persistent chemical differences between the craters, presumably reflecting differences in the shallow pathways for gas movement and escape. Scaling the results for $[X]_{tot}/SO_2$ by the time-averaged SO_2 flux (4500 t d^{-1}, 2.6×10^{10} mol a^{-1}) [*Allard*, 1997] suggests fluxes from Mt. Etna of 8×10^9 mol HF a^{-1} and 2×10^{10} mol HCl a^{-1}. These estimated fluxes of acidic gases from Mt. Etna are greater than the lower limits of earlier flux estimates of the global volcanic emissions of these species [*Symonds et al.*, 1988; *Halmer et al.*, 2002]. An increased flux of volcanic halogens to the troposphere may increase the potential for tropospheric ozone loss [e.g., *Vogt et al.*, 1996; *Bobrowski et al.*, 2007] and acid loading of local ecosystems [*Delmelle et al.*, 2002]. Our results for Br/Cl ($\sim$0.01) are generally higher than the mean value reported by *Aiuppa et al.* [2005a] (Br/Cl $\sim$ 0.001; from 52 filter packs collected January–October 2004). However, there is considerable variability in Br/Cl in both sets of data and so this discrepancy may reflect the larger sample size of *Aiuppa et al.* [2005a]. The explanation for such marked variability in the Br/Cl ratios in the Mt. Etna plume is unclear.

[30] SO_4^{2-}/SO_2 ratios were found to be $\sim$1% for the Voragine samples and $\sim$5% in NEC and downwind samples. The mechanism by which near-source volcanic sulfate is formed remains uncertain [*Allen et al.*, 2002; *Mather et al.*, 2006]. However, it may be due to the enhanced mixing of atmospheric O_2 with high-T magmatic gases in the vent promoted by the large open crater of NEC leading to increased homogeneous oxidation of SO_2 to SO_3, forming SO_4^{2-} by reaction with H_2O [*Martin et al.*, 2006; *Mather et al.*, 2006]. Also, if SO_4^{2-} is formed by low-T oxidation of SO_2, increased SO_4^{2-}/SO_2 at NEC may reflect the contribution from more aged plume (Figure 1). Results for Na^+/K^+ (0.3–18 μg μg^{-1}) and Na^+/Ca^+ (9–90 μg μg^{-1}) are consistent with the ranges reported previously for Mt. Etna's quiescent plumes [*Gauthier and Le Cloarec*, 1998; *Aiuppa et al.*, 2006; *Allen et al.*, 2006].

[31] Partitioning of elements and ions between gas and particles can be assessed using equation (9). Values of K were calculated from individual results in Tables 4a and 4b; mean K for F^-, Cl^-, and NO_3^- are given in Table 6.

$$K = \frac{[X]_{tot:particle}}{[X]_{tot:gas}} \tag{9}$$

Table 4b. Analysis of FP Samples: Acid Gas Filters[a]

Sample	Location	F^-	Cl^-	Br^-	NO_3^-	SO_4^{2-}
FP01A	NEC	490	770	28	0.19	950
FP02A	NEC	240	430	10	0.38	520
FP03A	VOR	390	500	57	0.33	1200
FP04A	VOR	130	490	17	0	1400
FP05A	NEC	480	1300	7.3	0.14	660
FP06A	DW	51	170	2.9	1.1	670
FP07A	DW	20	45	2.5	0.082	170
FP08A	BG	0	0.83	0	0.74	0.17
FP09A	VOR	46	380	0	1.3	980
FP10A	VOR	140	1300	0.067	2.3	2300
FP11A	NEC	150	530	2.7	1.4	470
FP12A	NEC	130	500	1.7	0.6	410
Mean	NEC (n = 5)	300	700	10	0.53	600
Mean	VOR (n = 4)	180	670	19	0.99	1500
Mean	DW (n = 2)	36	110	2.7	0.59	420

[a]The concentrations of ions in the plume, $[X]_{tot}$, are given in units of μmol m^{-3}. Measurement uncertainties are given in Table 2.

Table 5. Molar $[X]_{tot}/SO_2$ Ratios in the Plume of Mt. Etna[a]

Type	Location	F^-	Cl^-	Br^-	NO_3^-	SO_4^{2-}	Na^+	NH_4^+	K^+	Ca^{2+}
Particle	NEC (n = 5)	0.0039	0.0035	-	0.00094	0.049	0.023	0.0009	0.0027	0.00038
	VOR (n = 4)	0.0026	0.0012	-	0.00095	0.017	0.02	0.0014	0.0039	0.00019
	DW (n = 2)	0.022	0.021	-	0.0083	0.05	0.0086	0.0012	0.002	0.0002
Gas	NEC (n = 5)	0.46	1.2	0.014	0.0011	1	-	-	-	-
	VOR (n = 4)	0.13	0.44	0.015	0.00066	1	-	-	-	-
	DW (n = 2)	0.098	0.26	0.0095	0.0011	1	-	-	-	-

[a]Units are μmol μmol^{-1}. Calculated from the results in Tables 4a and 4b.

[32] F^- and Cl^- at the summit sites partition predominantly into the gas phase (i.e., $K < 1$) as gaseous hydrogen halides (HX). An increased amount of particulate F^- and Cl^- is present downwind. This latter observation may relate to plume evolution or to the meteorological conditions on the day of sampling. Table 6 shows that F^- partitions more strongly into the particle phase than Cl^-. A possible explanation is that HF condenses because ambient temperatures are close to the boiling point (T_b = 293 K at 1 atm). The formation of particulate F^- is unlikely to be driven by solubility and acid dissociation of HF in aqueous droplets as HF is a weak acid. In contrast, HCl is a strong acid so the formation of particulate Cl^- is likely driven by solubility and acid dissociation. The boiling point of HCl (T_b = 188 K) is too low for condensation to be a major process. The observation that significant amounts of Cl^- remain in the gas phase indicates that particle formation is limited by relative humidity and the availability of condensable water, consistent with other modeling and diffusion-tube data from Etna [*Aiuppa et al.*, 2007]. While it was not possible to determine $[X]_{tot}$ for particulate Br^-, the low boiling point of HBr (T_b = 207 K) and the relative abundance of Br^- in the gas phase suggests $K < 1$; this result is consistent with the conclusions of *Aiuppa et al.* [2005a].

[33] Filter pack samples showed some evidence of elevated NO_3^- in the plume in line with findings elsewhere (e.g., Masaya volcano, Nicaragua) [*Mather et al.*, 2004a] although concentrations were an order of magnitude less than measured at Masaya volcano. However, increased K for NO_3^- in the downwind samples (relative to NEC and VOR) suggests that oxidation of volcanogenic NO to HNO_3 does occur, albeit at a much slower rate than at Masaya.

4.2. MOUDI-IC

[34] MOUDI samples were analyzed to measure the concentration (ppm) of F^-, Cl^-, Br^-, NO_3^-, SO_4^{2-}, Na^+, NH_4^+, K^+, and Ca^{2+} in the extract solutions. These results were used to derive the concentration density distribution [X] using (3) (Table 7a). The concentrations of Br^-, NO_3^-, and Ca^{2+} in the MOUDI sample extracts were generally found to be <0.01 ppm and so results for these ions are not reported. A few values of [X] for K^+ (MD01/8, MD03/7, MD03/9) were found to be an order of magnitude larger than values from other stages in the same sample. These results for K^+ were assumed to be erroneous (i.e., due to contamination with K^+ or some other coeluting species) and so were replaced by the averages of adjacent values. Table 7b shows the total concentration of each ion in the plume (in the particle phase) found by summing [X] $d\log(d_a)$ over all stages.

[35] Figure 4 shows a clear elevation in SO_4^{2-} in both plumes relative to the background. The NEC samples show bimodal SO_4^{2-} with peaks at ~1 μm and ~8 μm whereas the Voragine samples show only the smaller of the two modes (~1 μm). This is consistent with observations reported by *Allen et al.* [2006] which showed the NEC plume had more SO_4^{2-} in the >3.5 μm fraction than the Voragine plume which had more SO_4^{2-} in the <3.5 μm fraction. This result suggests that the differences observed in the modality of sulfate aerosols between the summit vents are persistent. The ~8 μm mode in the NEC plume may reflect some contribution from more aged plume (allowing for increased particle growth). However, as sulfates are transported in the plume as a range of species (e.g., solid sulfates and aqueous droplets), the ~8 μm mode in the NEC plume may also represent a sulfate species which is absent from the Voragine plume or reflect a different balance in the two plumes between homogeneous nucleation and heterogeneous nucleation onto preexisting silicate particles.

[36] Figure 5 shows the size distribution of Na^+, K^+ and NH_4^+ in the plume calculated using (3). Na^+ and K^+ have modes in the >1 μm range consistent with transport as metal sulfates although the size distributions are less well defined than for SO_4^{2-} suggesting that Na^+ and K^+ also occur in other types of soluble particle (with differing size distributions). Previous studies show that Na^+ and K^+ are also transported as metal halides [*Varekamp et al.*, 1986]; this is consistent with our results (Table 7b) showing elevated particulate Cl^- and F^- within the plume relative to the background (although no distinct modes could be identified). NH_4^+ shows a mode at ~2 μm in MD05 which is not found in other samples. The large variability in the concentration of NH_4^+ in the plume is also found in results from filter packs (Table 4a). These observations may indicate a sampling artifact (e.g., NH_3 emitted by the authors during sampling), however, distance was maintained (>1 m) between the authors and the equipment throughout sampling to avoid resuspending dusts. A further possibility is contamination of MD05 with gas and aerosols emitted by the low-T fumaroles at the summit of Mt. Etna.

[37] The total concentration of ions in the plume measured by MOUDI-IC were compared with results from filter pack particle filters analyzed using IC. The concentration of

Table 6. Partition Coefficients for F^-, Cl^-, and NO_3^-[a]

Location	F^-	Cl^-	NO_3^-
NEC (n = 5)	0.0077	0.0032	2.1
VOR (n = 4)	0.038	0.0031	2.9
DW (n = 2)	0.23	0.079	13
BG (n = 1)	>1	0.36	1.4

[a]See equation (9). Partition Coefficients (K) > 1 indicates enrichment in the particle phase relative to the gas phase.

Table 7a. Concentrations of Ions in the Plume[a]

Stage	d_{50}*/μm	GM/μm	F^-	Cl^-	SO_4^{2-}	Na^+	NH_4^+	K^+
MD01/T	34	48	0.036	0.18	2.6	4.4	0.12	0.24
MD01/1	19	26	0.033	0.29	1.1	1.3	0.079	0.11
MD01/2	12	16	0.02	0.031	3.1	0.82	0.075	0.5
MD01/3	5.8	8.2	0.015	0.014	7.7	1.4	0.048	0.32
MD01/4	3.4	4.8	0.0086	0.038	1.4	1.2	0.38	0.069
MD01/5	1.9	2.7	0.014	0.01	3.1	0.33	0.14	0.19
MD01/6	1	1.5	0.0068	0.013	1.1	0.048	0.053	0.018
MD01/7	0.61	0.86	0.03	0.038	0.64	1.1	0.15	0.23
MD01/8	0.33	0.46	0.0068	0.0095	0.0049	3.5	0.19	0.13
MD01/9	0.19	0.26	0.013	0.0095	0.011	0.019	0.039	0.028
MD01/10	0.1	0.14	0.039	0.12	0.61	0.022	0.034	0.02
MD01/B	0.051	0.072	0.0018	0.27	0.00024	1.2	0.039	0.033
MD02/T	35	49	0.031	0.034	0.0016	0.032	0.032	0.13
MD02/1	19	27	0.042	0.021	0.0061	2.1	0.03	0.03
MD02/2	12	17	0.02	0.015	0.27	0.016	0.034	0.014
MD02/3	6	8.5	0.018	0.081	0.41	0.026	0.064	0.26
MD02/4	3.5	4.9	0.021	0.048	3	0.042	0.066	0.023
MD02/5	1.9	2.7	0.037	0.018	4.4	0.041	0.079	0.51
MD02/6	1.1	1.5	0.056	0.092	1.5	0.35	0.053	0.11
MD02/7	0.63	0.89	0.014	0.018	0.77	0.021	0.051	0.086
MD02/8	0.34	0.48	0.031	1.1	0.63	0.035	0.056	0.02
MD02/9	0.19	0.27	0.032	0.26	0.27	0.028	0.045	0.017
MD02/10	0.1	0.15	0.03	0.18	0.0012	0.018	0.039	0.011
MD02/B	0.052	0.074	0.054	0.26	0.24	1	0.056	0.011
MD03/T	35	49	0.1	0.29	2.6	0.69	0.067	0.2
MD03/1	19	27	0.044	0.039	2.7	0.026	0.049	0.017
MD03/2	12	17	0.00098	0.13	5.6	1.2	0.047	0.32
MD03/3	6	8.5	0.053	0.046	11	1.9	0.039	0.46
MD03/4	3.5	4.9	0.026	0.37	8.7	1.4	0.063	0.78
MD03/5	1.9	2.7	0.041	0.1	3.4	0.042	0.048	0.3
MD03/6	1.1	1.5	0.13	0.49	6.7	0.081	0.18	0.11
MD03/7	0.63	0.89	0.028	0.038	2	0.042	0.05	0.066
MD03/8	0.34	0.48	0.081	0.11	0.34	0.12	0.073	0.025
MD03/9	0.19	0.27	0.00098	0.38	0.36	0.045	0.034	0.024
MD03/10	0.1	0.15	0.072	0.047	0.016	0.03	0.041	0.023
MD03/B	0.052	0.074	0.19	0.11	0.24	1.8	0.041	0.037
MD04/T	33	46	0.022	0.0081	0.0059	0.056	0.0086	0
MD04/1	18	26	0.012	0.009	0.0032	0.011	0.0084	0.01
MD04/2	11	16	0.013	0.011	0.0063	0.24	0.025	0.34
MD04/3	5.7	8	0.011	0.01	0.0045	0.014	0.0071	0.0066
MD04/4	3.3	4.6	0.0029	0.08	0.006	0.029	0.022	0.033
MD04/5	1.8	2.6	0.032	0.16	0.0039	0.019	0.017	0.35
MD04/6	1	1.4	0.013	0.013	0.39	0.0075	0.19	0.013
MD04/7	0.59	0.84	0.017	0.12	0.14	0.021	0.092	0.0065
MD04/8	0.32	0.45	0.012	0.068	0.0054	0.0045	0.012	0.53
MD04/9	0.18	0.26	0.028	0.0099	0.0053	0.017	0.01	0.013
MD04/10	0.099	0.14	0.0094	0.038	0.0047	0.0082	0.0083	0.0059
MD04/B	0.049	0.07	0.039	0.078	0.0035	0.4	0.013	0.007
MD05/T	44	62	0.1	0.33	0.029	0.039	0.074	0.037
MD05/1	24	34	0.075	0.66	0.0054	0.025	0.099	0.022
MD05/2	15	21	0.18	0.9	0.032	0.48	0.26	0.13
MD05/3	7.6	11	0.063	0.022	0.012	9.5	0.2	0.048
MD05/4	4.4	6.2	0.19	0.42	1.6	2.5	0.27	0.87
MD05/5	2.4	3.5	0.0045	0.015	10	0.15	0.6	0.076
MD05/6	1.3	1.9	0.068	0.064	12	0.4	1.7	0.11
MD05/7	0.8	1.1	0.059	0.042	1.3	0.12	0.45	0.056
MD05/8	0.43	0.61	0.043	0.93	0.5	0.18	0.26	0.1
MD05/9	0.24	0.34	0.1	0.61	0.023	0.081	0.11	0.043
MD05/10	0.13	0.19	0.039	0.081	0.03	0.12	0.078	0.13
MD05/B	0.066	0.094	0.17	0.49	0.012	0.03	0.11	0.081
FL01/T	31	44	18	23	1.2	1.5	68	0.74
FL01/1	17	24	5.3	5.5	0.29	0.66	17	0.25
FL01/2	11	15	5.6	5.2	0.19	0.85	14	0.26
FL01/3	5.4	7.6	3.3	12	0.2	0.7	20	0.23
FL01/4	3.1	4.4	2.9	62	0.37	0.89	190	0.65
FL01/5	1.7	2.4	15	630	6.6	5.5	960	2.3
FL01/6	0.95	1.3	35	1300	3.7	12	3700	12
FL01/7	0.56	0.8	35	1100	2.8	21	3100	14
FL01/8	0.3	0.43	1.2	51	0.17	1.4	140	0.62
FL01/9	0.17	0.24	0.033	3.6	0	1.4	50	0.73
FL01/10	0.094	0.13	0.8	12	0.042	0.5	26	0.4

[a][X] (μmol m^{-3}), from MOUDI-IC. The cutoff diameters (d_{50}*) shown are corrected for flow rate. Also given is the geometric midpoint (GM) of each size interval. Suffixes denote the MOUDI stage, e.g., T = Top, B = Backup, 1–10 = numbered stages.

Table 7b. Total Concentration of Each Ion in the Plume[a]

Sample	F^-	Cl^-	SO_4^{2-}	Na^+	NH_4^+	K^+
MD01	0.068	0.31	6.4	4.6	0.41	0.57
MD02	0.12	0.64	3.5	1.1	0.18	0.37
MD03	0.23	0.65	13	2.2	0.22	0.71
MD04	0.064	0.18	0.17	0.25	0.12	0.4
MD05	0.33	1.4	7.7	4.1	1.3	0.52
FL01	37	960	4.7	14	2500	9.7

[a]In the particle phase, found by summing [X] $d\log(d_a)$ over all MOUDI stages (equation (8)). Results are given as μmol m^{-3}.

ions in the plume was generally found to be higher when measured using the filter packs. This is consistent with the filter packs being deployed for short durations when the wind was blowing the plume over the sampling site. In contrast, the MOUDI-IC sampled continuously for 2–3 h and so sampled a higher proportion of relatively clean air. The only samples made simultaneously for comparable durations were MD05 and FP09; in this case, the concentrations of ions measured are in good agreement. F^- is exceptional and shows much higher concentrations in FP09 than in MD05. This difference may indicate that HF drawn through the filters in FP-IC reacts with, or condenses onto the filter, or particles on the filter. This result suggests that the partition coefficient for F^- (i.e., K(F); Table 6) may have been overestimated (although HF condensation as a mechanism for particulate F^- remains applicable).

[38] Results for the sample (FL01; Tables 7a and 7b) collected above a degassing fracture in a fresh lava flow [e.g., *Andronico et al.*, 2005] show a single dominant particle phase at <1 μm; the small size of particles may reflect the very young age of the plume (~1–2 s) with insufficient time for significant particle growth (assuming that particle formation occurs primarily upon cooling at the fracture opening). The plume sampled here is also highly concentrated relative to the more dilute plumes sampled at the crater rim. The total concentration of particulate Cl^- was 960 μmol m^{-3}; assuming an upper limit of K(Cl) ~ 0.003 (Table 6) we estimate the concentration of HCl gas was at least 0.3 mol m^{-3} representing a clear respiratory hazard. SO_4^{2-} was found to be a minor component of the fracture plume; this is consistent with most of the SO_2 being degassed from the magma prior to eruption or soon afterward, near the eruptive vent. The fracture plume also showed very high levels of NH_4^+ suggesting the presence of NH_4Cl; the crystalline form, sal ammoniac, is a common incrustation on fresh lava surfaces [e.g., *Óskarsson*, 1981]. It is unclear whether this NH_4^+ is derived from pyrolysis of organic materials overrun by the lava flow; from magmatic NH_3 [e.g., *Naughton et al.*, 1974; *Rose et al.*, 1986] or from atmospheric NH_3 [*Mather et al.*, 2003a].

4.3. FP-QEMSCAN: Silicate Particles

4.3.1. Number Density Distribution

[39] Previous studies have identified fine silicate particles (modal $d \sim 1$ μm) in the Mt. Etna [*Lefevre et al.*, 1986] and Kilauea [*Meeker and Hinkley*, 1993] plumes. These fine silicates were generally found to be spherical, indicating that fine silicates do not self-coagulate in the plume. This is consistent with the low abundance of fine silicates and also the narrow size range spanned by the fine silicate particle size distribution [e.g., *Lefevre et al.*, 1986]; both of these factors inhibit self-coagulation [*Hinds*, 1999]. The rate law of *Gislason and Oelkers* [2003] suggests the dissolution of fine silicates in acidic droplets (at 298 K) would occur over timescales of days, rather than minutes. Hence, coagulation and dissolution processes would not be expected to affect the size of silicate particles between emission and collection.

[40] Figure 6 shows $N(d)$ for silicate particles from samples QM01–QM03 in the size range $0.1 < d/\mu m < 10$ (i.e., by our definition, $N(d)$ for fine silicate particles). In the calculation of $N(d)$ no distinction was made between metal-rich and metal-poor fine silicates. All samples show a modal particle diameter of $d \sim 1.4$ μm. The sharp decrease in $N(d)$ below ~0.5 μm is an artifact of instrumental limitations and the onset of significant losses of particles through the pores

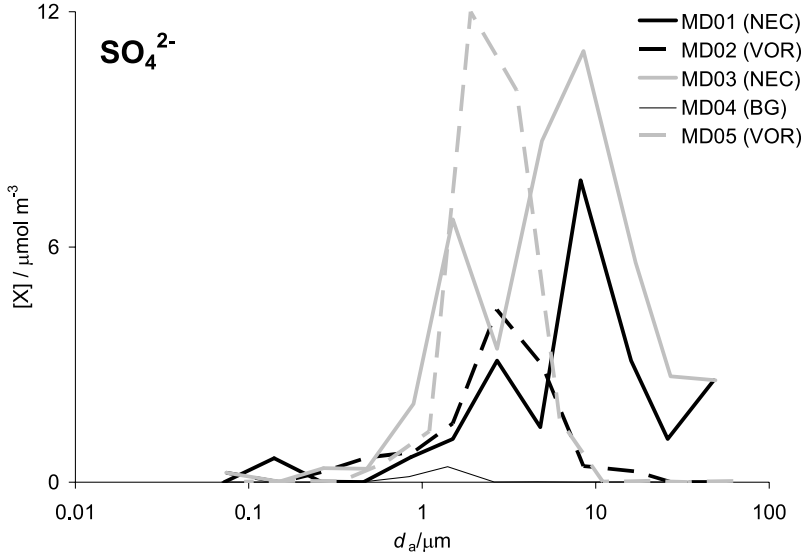

Figure 4. [X] (μmol m^{-3}) for SO_4^{2-} from the impactor.

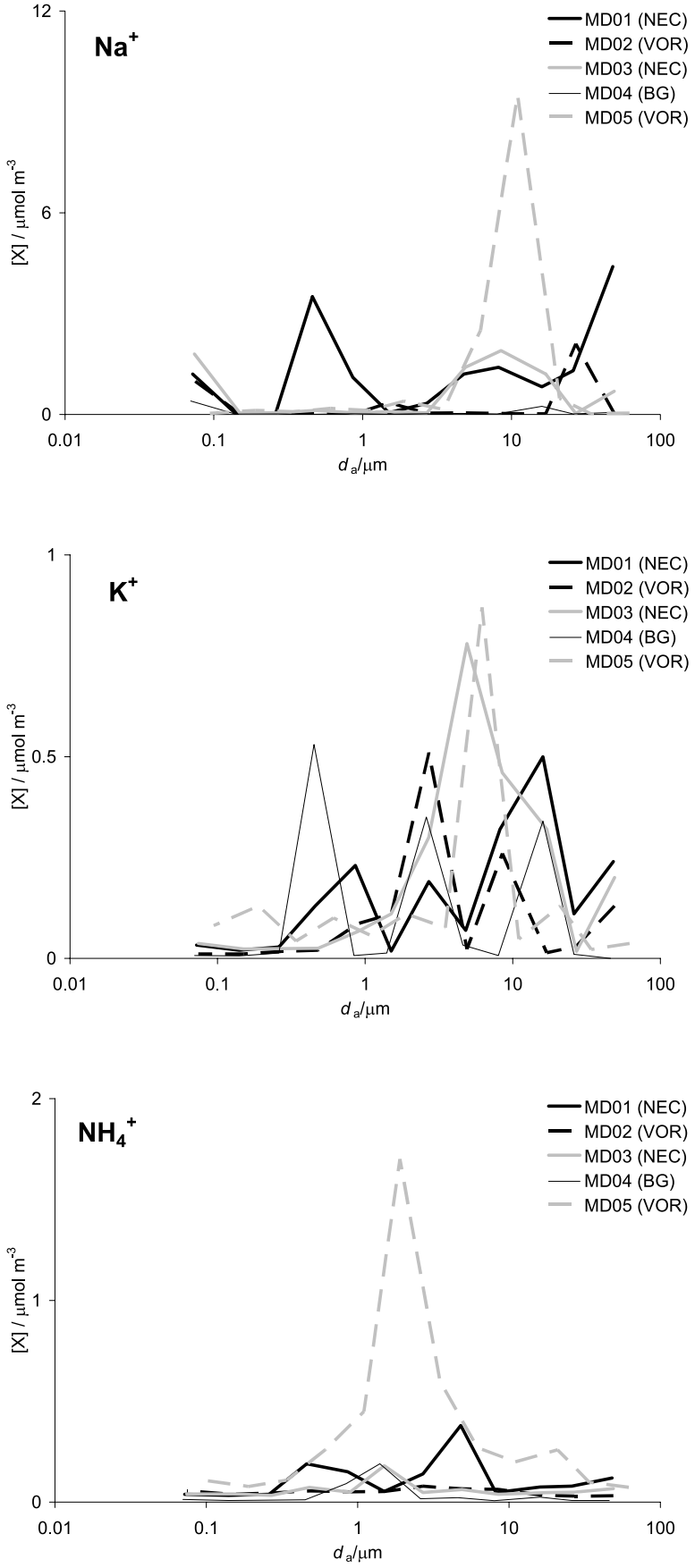

Figure 5. [X] (μmol m^{-3}) for Na^+, K^+, and NH_4^+ from the impactor.

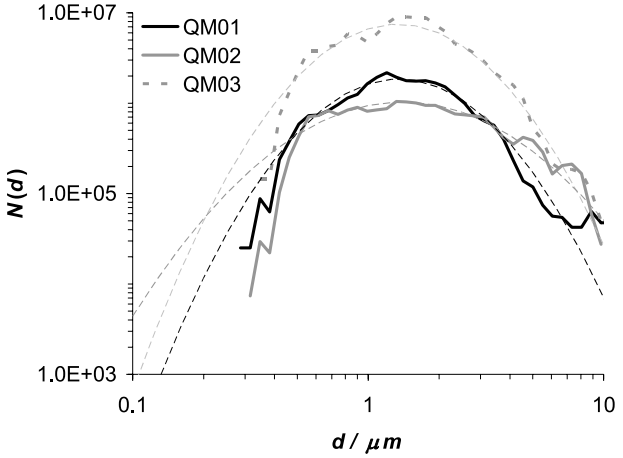

Figure 6. $N(d)$ (m^{-3}) for fine silicates in the North East Crater (QM01) and Voragine plumes (QM02, QM03) calculated from the QEMSCAN data. The lognormal fit is given by dashed lines.

($d \sim 0.8$ μm). $N(d)$ for fine silicates were found to be approximately lognormal in all cases; this strongly suggests that all silicate particles in the size range $0.1 < d/\mu m < 10$ are formed by a single emission process (irrespective of whether they are identified by QEMSCAN as metal-poor or metal-rich). Furthermore, a lognormal $N(d)$ also indicates that the evolution of particles from a metal-rich to a metal-poor composition does not result in significant changes in particle size. It should be noted that these results do not preclude larger ($d > 10$ μm) silicate particles forming through other processes (e.g., Pele's hairs and tears) [*Moune et al.*, 2007].

[41] The number density distribution, $N(d)$, is described by equation (10) with shape parameters, σ_N and μ_N, and the amplitude parameter N'

$$N(d) = \frac{N'}{\sigma_N\sqrt{2\pi}} \exp\left(-\frac{1}{2}\left(\frac{\log(d) - \mu_N}{\sigma_N}\right)^2\right) \qquad (10)$$

[42] This parameterization of the lognormal distribution was chosen to maintain consistency with the logarithmic definition of $N(d)$ (3) commonly used in aerosol studies [e.g., *Watson and Oppenheimer*, 2000, 2001; *Allen et al.*, 2006]. The parameters μ_N and σ_N are equivalent to the mean and standard deviation of the distribution in $\log(d)$ space. The relationships between these parameters and summary statistics in d (e.g., mode and standard deviation) are more complex, however, the modal diameter (d_N*) is simply the inverse logarithm of μ_N (i.e., $\mu_N = \log d_N$*). The parameter N' is equivalent to the total number of particles in the distribution per cubic meter of plume.

[43] The lognormal parameters were calculated for QM01 − QM03 between $0.5 < d/\mu m < 4$ (Figure 6 and Table 8). This fitting window was chosen because $N(d)$ for $d > 4$ μm in QM01 cannot be described by the same distribution as for $d < 4$ μm. There are fewer particles with $4 < d/\mu m < 8$ in QM01 than predicted by the lognormal distribution which may indicate a tendency for larger particles to be lost from the NEC plume by deposition. The terminal settling velocity in still air for a 10 μm spherical silicate particle (assuming a density of 2800 kg m^{-3}) [*Lefevre et al.*, 1986] is 0.0087 m s^{-1} [*Hinds*, 1999] and so gravitational settling can be excluded. However, the large open crater at NEC promotes swirling which may lead to inertial impaction of particles onto the walls and bottom of the crater. The peak in $N(d)$ for QM01 around $d \sim 10$ μm may be related to the audible magma spattering explosions, although as only six particles were measured it is difficult to interpret this result. $N(d)$ for QM02 and QM03 is well described by a lognormal distribution indicating that fine silicates in the Voragine plume are not lost by deposition prior to collection.

[44] The increased width of the distribution (i.e., σ is greater) in QM02 compared to QM03 suggests some time variation in the physical parameters governing the emission of fine silicates from the Voragine vent. It could be suggested that fine silicates are formed by bubbles bursting on the surface of the magma, generating a spray of silicate droplets. Studies of bubbles bursting in salt water [*Russell and Singh*, 2006] and gas/iron/slag systems [*Han and Holappa*, 2001, 2003] report bimodal particle size distributions with large quantities of film droplets (in a lognormal distribution centered around $d \sim 1$ μm; ~100 film droplets per bubble) produced by rupture of the bubble film and a smaller number of large jet droplets produced by collapse of the cavity left on the surface of the liquid after bursting. These studies have gone some way to elucidating the relationships between particle size distributions, bubble size distributions and properties of the liquid (e.g., viscosity and surface tension). If fine silicates are formed by bursting bubbles, understanding these relationships may offer new insights into the physical processes occurring at the surface of the magma.

[45] N' can be identified as the number of fine silicates per cubic meter of plume that would be measured in the absence of deposition effects, underdetection by the instrument, or losses through the pores. This approach assumes that the distribution remains lognormal outside the fitting window. However, as the vast majority of particles are within the fitting window, N' and the actual number of particles

Table 8. Lognormal Parameters for $N(d)$ for QM01, QM02, and QM03[a]

Sample	Location	N'/particles m^{-3}	μ_N	σ_N	d_N*/μm	$V'/\mu m^3$ m^{-3}	μ_V	σ_V	d_V*/μm
QM01	NEC	1.2×10^6	0.14	0.25	1.38	7.3×10^6	0.57	0.25	3.73
QM02	VOR	9.0×10^5	0.15	0.36	1.41	2.9×10^7	1.05	0.36	11.1
QM03	VOR	5.4×10^6	0.14	0.25	1.38	3.3×10^7	0.58	0.25	3.73

[a]Units for $N(d)$ are m^{-3}. Also given are the lognormal parameters for $V(d)$ (units are μm^3 m^{-3}) derived using (11a)–(11d). The parameters μ_N and σ_N are equivalent to the mean and standard deviation of the $N(d)$ distribution in $\log(d)$ space; μ_V and σ_V are defined equivalently in terms of $V(d)$.

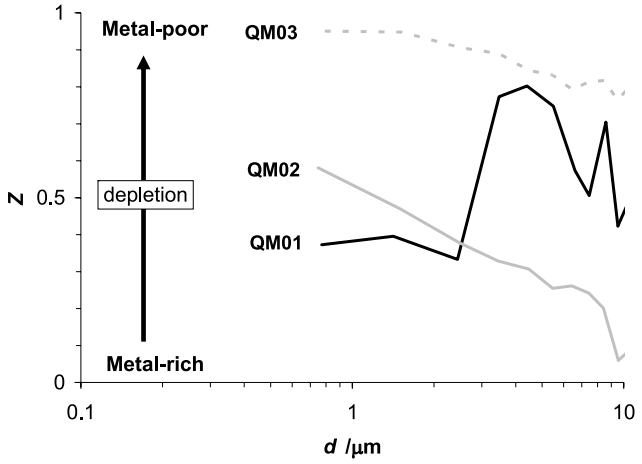

Figure 7. Chemical depletion of fine silicates calculated from the QEMSCAN data. $Z = 1$ would indicate that all silicate particles of a given size were metal-poor. QM01 is the sample taken from North-East Crater plume in 2005. QM02 is the sample taken from the Voragine plume in 2005. QM03 is the sample taken from the Voragine plume in 2004.

detected are in fact approximately equivalent. IC analysis of FP01A and FP03A show the concentrations of SO_2 during sampling of QM01 and QM02 were 950 μmol m^{-3} and 1200 μmol m^{-3}, respectively (Table 4b). Assuming N'/SO_2 is approximately constant within the plume over time, scaling by the emission flux of SO_2 (4500 t d^{-1}, 2.6×10^{10} mol a^{-1}) *Allard* [1997] gives the emission flux of fine silicates from Mt. Etna as $\sim 10^{12}$ particles s^{-1}. If the fine silicates are formed by bursting bubbles, the large magnitude of this flux indicates that the emission process is continuous (i.e., due to the bursting of large numbers of small bubbles) rather than discrete (i.e., from the bursting of large gas slugs at the top of the conduit).

[46] The volume density distribution, $V(d)$, is also lognormal. It can be shown using calculus that the statistical parameters of $V(d)$ (σ_V, μ_V, V') are related to σ_N, μ_N and N' by equations (11a)–(11d); results for σ_V, μ_V and V' are given in Table 8.

$$V(d) = \frac{V'}{\sigma_V \sqrt{2\pi}} \exp\left(-\frac{1}{2} \left(\frac{\log(d) - \mu_V}{\sigma_V} \right)^2 \right) \tag{11a}$$

$$\sigma_V = \sigma_N \tag{11b}$$

$$\mu_V = 3 \ln 10 \sigma_N^2 + \mu_N \tag{11c}$$

$$V' = \frac{\pi}{6} N' \exp\left(\frac{1}{2} \left[\{3\sigma_N \ln 10\}^2 + 6\mu_N \ln 10 \right] \right) \tag{11d}$$

[47] Table 8 shows $V' \sim 10^7$ μm^3 m^{-3}, suggesting a fine silicate particle flux from Mt. Etna of around 7000 kg d^{-1} (assuming a density of 2800 kg m^{-3}) [*Lefevre et al.*, 1986]. *Lefevre et al.* [1986] estimated a fine silicate flux from Mt. Etna of $\sim$1600 kg d^{-1}. The increased magnitude of our estimated flux may reflect temporal differences in the activity of Mt. Etna, however, it is also possible that this previous study underestimated the flux of fine silicates by assuming that all particles have an equal diameter. The mass flux of fine silicates is dwarfed by the 5×10^7 kg d^{-1} of fine ash ($d \sim 10$ μm) emitted globally by small volcanic eruptions [*Mather et al.*, 2003b]. However, this flux of fine silicates ($d \sim 1$ μm) remains important because of the extended atmospheric lifetime of these particles (relative to larger ash particles) increasing the potential for long-range atmospheric transport. Measurements of fine silicates in ice cores may therefore prove useful indicators of the extent of persistently active volcanism over time [e.g., *Gaudichet et al.*, 1988].

4.3.2. Composition

[48] Figure 7 shows the variation in the fraction of metal-poor fine silicates, Z, with particle size. Fine silicates in the Voragine samples (QM02 and QM03) become increasingly metal-rich with increasing particle size. In contrast, the NEC sample (QM01) shows that largest particles are the most metal-poor (i.e., highest Z). There were $\sim$150 particles with $d > 4$ μm measured on QM01 and so this result is significant.

[49] These results are consistent with previous studies identifying fine silicate particles (modal $d \sim 1$ μm) in volcanic plumes with compositions ranging from magmatic to nearly pure silica [*Lefevre et al.*, 1986; *Meeker and Hinkley*, 1993]. Coarse silicate particles ($d > 50$ μm) from Masaya were often found to have a metal-poor surface layer of thickness $\sim$10 μm [*Moune et al.*, 2007]. In other work, *Spadaro et al.* [2002] exposed basaltic glass to dilute Mt. Etna plume (from Bocca Nuova vent; Figure 1) and showed that reactions lead to depletion of metals to depths of 10 μm on the timescale of days. Several mechanisms for the formation of metal-poor fine silicates can be suggested [*Lefevre et al.*, 1986; *Delmelle et al.*, 2007]: (1) reactions between silicate particles and acidic droplets, (2) reactions between silicate particles and high-T gases, (3) precipitation of silicates from Si-rich aqueous droplets, and (4) reactions in the magma.

[50] The lognormal $N(d)$ of fine silicates strongly indicates that metal-poor and metal-rich particles are emitted from the magma by a single process. This constraint excludes precipitation from Si-rich droplets which would likely result in a more complicated particle size distribution. The presence of metal-poor silicates in the bulk magma can also be excluded because none of Mt. Etna's recent volcanic products have been saturated in quartz [*Allard et al.*, 2006]. A further possibility is the reaction of sulfur with silicates in the magma leading to the production of sulfides, oxides and silica [*Lefevre et al.*, 1986]. If this reaction formed an emulsion between metal-rich and metal-poor silicate liquids, it is feasible that the bursting of bubbles could generate a lognormal particle size distribution. However, the melting point of silica is $\sim$1700°C and so silica would form as a solid in the Mt. Etna magma ($\sim$1140°C). Therefore, there would be no relationship between the size distributions of metal-rich and metal-poor fine silicates. It seems extremely unlikely that two independent and unrelated particle size distributions would sum to give a lognormal distribution. Inspection of the QEMSCAN index files for each sample

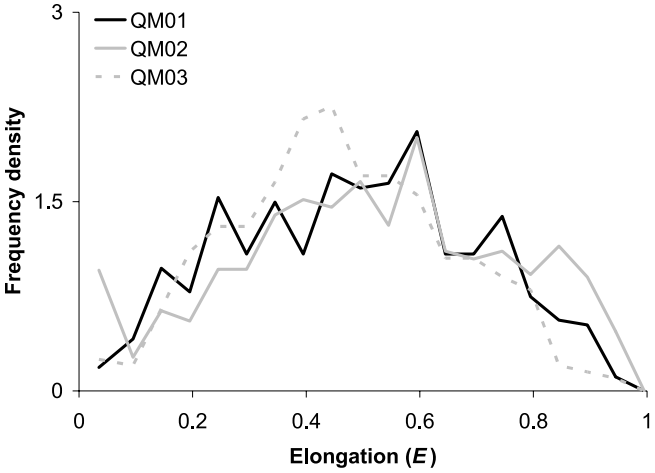

Figure 8. Elongation, E, calculated from the QEMSCAN data for fine silicates in the North East Crater (QM01) and Voragine plumes (QM02, QM03).

(e.g., Figure 2; QM02) offers an additional constraint; fine silicates are generally entirely metal-poor or entirely metal-rich (rather than zoned). This result is inconsistent with the reaction of fine silicates with high-T gases because such reactions would presumably affect all particles of a similar size equally (resulting in a sharp transition between metal-poor and metal-rich particles at some critical d). Of the suggested mechanisms, these results are therefore only consistent with differentiation occurring after emission from the magma, due to coagulation and reaction of fine silicates with acidic droplets.

[51] The variation in Z for QM02 and QM03 can be rationalized as follows. If depletion occurs from the surface of fine silicates, particles will be identified as metal-poor (by QEMSCAN) if the depth of depletion is comparable to the size of the particle. The likelihood of this condition being satisfied will decrease with increasing particle size. The differences between QM02 and QM03 reflect increased relativity humidity during sampling of QM03; high RH promotes the formation of larger and more acidic droplets, leading to more significant depletion of metals from fine silicates. The variation in Z for QM01 is consistent with deposition of larger fine silicates (i.e., $d > 3-4$ μm) from the NEC plume. If these larger fine silicate particles are subsequently resuspended, the extended exposure time to the plume is manifest as an increase in Z.

4.3.3. Elongation

[52] Figure 8 shows a frequency density curve for particle elongation (normalized to unity) of fine silicates ($d < 10$ μm) in the Mt. Etna plumes (QM01–QM03). The most common particle elongation is $E \sim 0.5-0.6$ but significant proportions of particles are more or less elongated. The modal elongation in all samples corresponds to the major axis being ~50% longer than the minor axis. These results suggest the viscosity of the melt is too high for ejected melt droplets to assume spherical geometry to minimize surface tension before freezing occurs. The nonspherical shape of fine silicates particles introduces uncertainty into our calculations of the mass flux as we assume the depth axis (c) of particles is equal to d. If prolate geometry ($a > b = c$) is more appropriate, the calculated mass flux may be slightly overestimated and should be adjusted downward by ~20% (i.e., 5600 kg d^{-1}). No correlations were found between E and d in any sample suggesting that particle shape becomes fixed at the instant a frozen crust forms on the particle.

4.4. FP-QEMSCAN: S-Rich Particles

4.4.1. Sulfur and Sulfides

[53] Elemental sulfur and iron-rich sulfides (Fe-S) were detected by QEMSCAN. The compositional maps suggest these two phases generally occur together in single particles and so it seems likely that the best chemical description for these particles is S-rich with a variable concentration of metal ions (Fe and other metal ions in smaller amounts).

[54] A potential route to elemental sulfur is the reaction (R1) of H_2S and SO_2 which is favored by cooling of high-temperature volcanic gases emitted at the active vent [*Giggenbach*, 1987].

$$2H_2S + SO_2 = 2H_2O + 3/2\ S_2 \quad \text{(R1)}$$

[55] This reaction will not affect the validity of the scaling approach used previously because $SO_2/H_2S \sim 20$ in the Mt. Etna plumes [*Aiuppa et al.*, 2005b]. The number density distribution, $N(d)$, was calculated for sulfur/sulfide particles and is shown in Figure 9 for QM01–QM03 in the range 0.1 μm $< d < 10$ μm. In all three samples, the sulfur/sulfide particles appear to have a mode ~0.5 μm; given the detection limit of the instrument we cannot rule out that $N(d)$ continues to increase at lower particle size. $N(d)$ for sulfur/sulfide decreases more sharply in QM01 than in other samples.

[56] The emission of sulfur/sulfide particles into the environment is significant. In crystalline form, FeS_2 (pyrite) is known to have catalytic properties and so emission may have important biological and atmospheric implications [*Cohn et al.*, 2006]. Furthermore, these sulfide particles are likely to be significantly enriched in chalcophile elements, including As, Cd, Cu, Mo, Tl, Zn, Hg. Emission of these trace elements as sulfides may have environmental

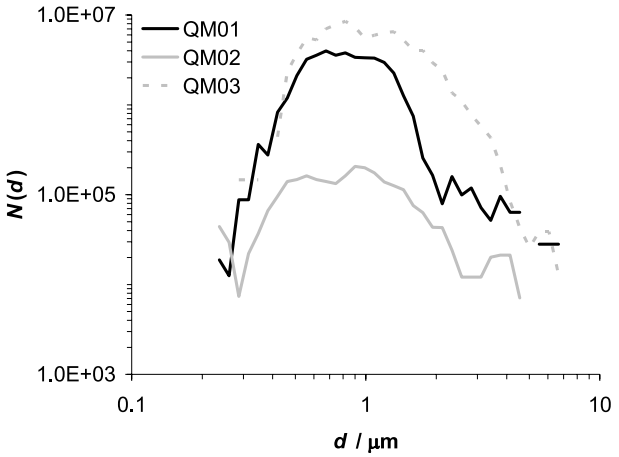

Figure 9. $N(d)$ (m^{-3}) for elemental sulfur and sulfides calculated from the QEMSCAN data in the North East Crater (QM01) and Voragine plumes (QM02, QM03).

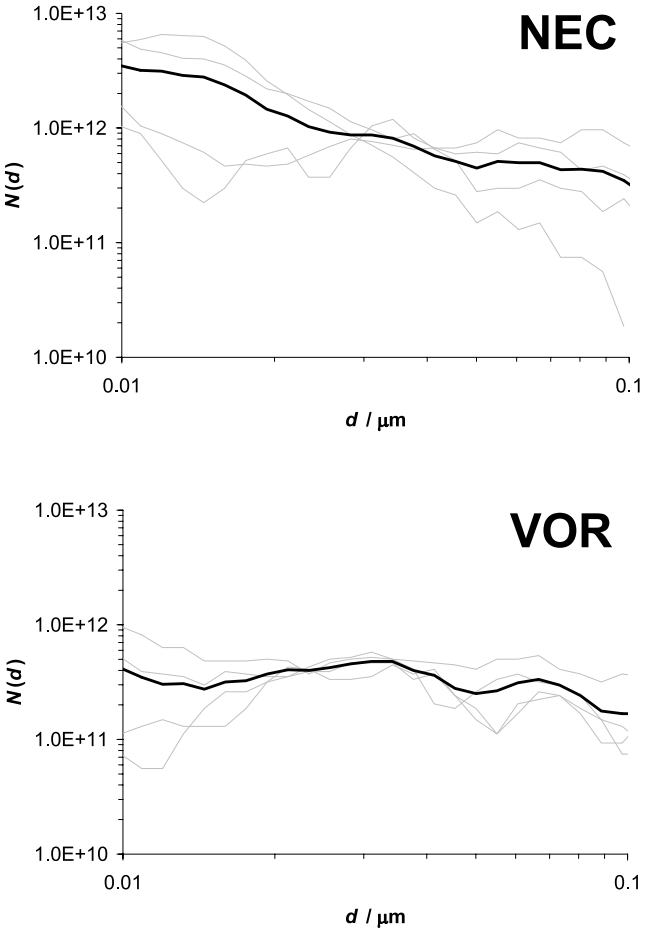

Figure 10. $N(d)$ for nanoparticles calculated from STEM data in the NEC (TP01) and Voragine plumes (TP02). Results for individual particle fields are given (narrow lines) as well as the mean (bold line).

implications as sulfides are generally less soluble than halides or sulfates, and may offer a mechanism for the long-range transport and preservation of the geochemical signature of semivolatile metals from degassing volcanoes [e.g., *Matsumoto and Hinkley*, 2001].

4.4.2. Sulfates

[57] FP-QEMSCAN results (e.g., Figure 2) show that sulfate is strongly associated with Ca^{2+}, Na^{+}, K^{+} and Al^{3+} within single particles; this is a stronger statement than possible from MOUDI-IC results where associations can only be inferred by comparisons of size distributions. However, comparison of results from FP-QEMSCAN and FP-IC suggest the detection of sulfates by QEMSCAN is not quantitative. This is because a significant fraction of sulfate in plume is dissolved in aqueous droplets and escapes detection by precipitation into the filter, rather than onto the surface.

4.5. TP-STEM

[58] The results from the analysis of TP samples with scanning transmission electron microscopy are shown in Figure 10 (derived using (6b)). For NEC (TP01), mean $N(d)$ increases between 10 nm – 40 nm although some variation was found between particle fields (dashed lines). For Voragine (TP02), mean $N(d)$ is a much weaker function of particle diameter for all fields.

[59] *Maynard* [1995] suggests that particle collection efficiency decreases above 40 nm in diameter but no change of gradient was found in either sample; this observation suggests that the stated limits on collection efficiency of the instrument are overly conservative or that increasing particle numbers of an unidentified insoluble particle phase above this diameter offset this effect. The general increase in $N(d)$ at lower d (for NEC) would suggest that gas-to-particle conversion generates large numbers of particles at <10 nm which grow by coagulation, or by condensation of gases.

[60] An estimate can be made of the flux of nanoparticles from Mt. Etna. Integrating $N(d)$ between limits of 10 nm and 100 nm suggests the plume contains $\sim 10^{12}$ nanoparticles m^{-3} at the crater rim. From Table 4b, the mean concentration of SO_2 at the crater rim is $\sim$1000 μmol m^{-3}. Scaling for the SO_2 flux (4500 t d^{-1}, 2.6×10^{10} mol a^{-1}) [*Allard*, 1997] yields a flux of $\sim 10^{18}$ nanoparticles s^{-1}. The atmospheric implications for this flux cannot be predicted without knowledge of the composition of these nanoparticles. However, if the nanoparticles were predominantly sulfate aerosols it seems likely that a significant fraction would be activated as cloud condensation nuclei (CCN) for conditions of >0.25% supersaturation (based on the calculations for sulfate aerosols of *Mather et al.* [2004b]). The large numbers of particles in the 10–100 nm size range in volcanic emissions may suggest that almost all the potential for volcanoes to emit CCN's lies within this size range although further modeling of the subsequent microphysics and especially coagulation behavior would be needed to confirm this.

5. Conclusions

[61] Volcanic plumes are a complex mixture of gas and particles which evolve over a range of timescales and any characterization study can only offer a "snapshot" of plume chemistry at a specific time. However, studies such as this provide a valuable insight into the processes occurring at the magma surface, in the vent and finally in the crater immediately prior to measurements.

[62] The soluble-ion chemistry of the plume was investigated using micro-orifice uniform deposition impactor (MOUDI) and filter pack samples taken at the summit of Mt. Etna and analyzed using ion chromatography. This work reveals that near-source volcanic sulfate in the NEC plume is transported in two distinct modes (at $\sim$1 μm and $\sim$8 μm) whereas the Voragine plume consists of a single sulfate mode (at $\sim$1 μm). Na^{+} and K^{+} generally have modes in the >1 μm range although they are not as well defined as those detected for sulfate. This result is consistent with the presence of several different Na^{+} and K^{+} bearing species (e.g., sulfates and halides) in the Mt. Etna plumes.

[63] QEMSCAN enables the detection and measurement of insoluble species in the volcanic plume. We estimate the emission flux of fine silicates ($d < 10$ μm) from Mt. Etna to be $\sim$7000 kg d^{-1}. The number density distribution of fine silicates follows a lognormal distribution consistent with a single source of particles; this may be the bursting of bubbles at the surface of the magma. This study also found

a significant proportion of fine silicates are depleted in metals relative to the magma. Our results are consistent with metal depletion occurring due to coagulation of fine silicate particles with acidic droplets in the plume. Studies of fine silicate particles may therefore offer insights into processes occurring at the surface of the magma, and also processes occurring in the vent and plume.

[64] Analysis of particles in the range 0.01 μm < d < 0.1 μm show that there are significant levels of nanoparticles in the Mt. Etna plumes. We estimate an emission flux of $\sim 10^{18}$ nanoparticles s^{-1}. If these particles are sulfates, this would constitute a significant source of cloud condensation nuclei (CCN) to the atmosphere.

[65] This study illustrates how the concurrent use of several techniques can offer the most comprehensive surveys of particle size distributions in volcanic plumes. The techniques developed here can readily be applied to other volcanoes.

[66] **Acknowledgments.** RSM thanks the Natural Environment Research Council for a PhD studentship, research costs and travel support and Magdalene College, Cambridge for further travel support. RSM also thanks Pierre Delmelle and Marie Edmonds for their comments on an earlier version of this manuscript. TAM thanks the Royal Society, and DMP thanks the Leverhulme Trust, for additional support. CJH thanks Ed Llewellin for useful discussions. The authors would also like to thank INGV for their much appreciated assistance in the field. The authors also thank three anonymous reviewers for insightful comments on earlier versions of this manuscript.

References

Abramoff, M. D., P. J. Magelhaes, and S. J. Ram (2004), Image Processing with ImageJ, *Biophotonics Int.*, *11*, 36–42.

Aiuppa, A., G. Dongarra, M. Valenza, C. Federico, and G. Pecoraino (2003), Degassing of trace volatile metals during the 2001 eruption of Etna, in *Volcanism and the Earth's Atmosphere*, *Geophys. Monogr. Ser.*, vol. 139, edited by A. Robock, and C. Oppenheimer, pp. 41–44, AGU, Washington, D. C.

Aiuppa, A., C. Federico, A. Franco, G. Giudice, S. Gurrieri, S. Inguaggiato, M. Liuzzo, A. J. S. McGonigle, and M. Valenza (2005a), Emission of bromine and iodine from Mount Etna volcano, *Geochem. Geophys. Geosyst.*, *6*, Q08008, doi:10.1029/2005GC000965.

Aiuppa, A., S. Inguaggiato, A. J. S. McGonigle, M. O'Dwyer, C. Oppenheimer, M. J. Padgett, D. Rouwet, and M. Valenza (2005b), H_2S fluxes from Mt. Etna, Stromboli, and Vulcano (Italy) and implications for the sulfur budget at volcanoes, *Geochim. Cosmochim. Acta*, *69*, 1861–1871, doi:10.1016/j.gca.2004.09.018.

Aiuppa, A., S. Bellomo, L. Brusca, W. D'Alessandro, R. Di Paola, and M. Longo (2006), Major-ion bulk deposition around an active volcano (Mt. Etna, Italy), *Bull. Volcanol.*, *68*, 255–265, doi:10.1007/s00445-005-0005-x.

Aiuppa, A., A. Franco, R. von Glasow, A. G. Allen, W. D'Alessandro, T. A. Mather, D. M. Pyle, and M. Valenza (2007), The tropospheric processing of acidic gases and hydrogen sulphide in volcanic gas plumes as inferred from field and model investigations, *Atmos. Chem. Phys.*, *7*, 1441–1450.

Allard, P. (1997), Endogenous magma degassing and storage at Mount Etna, *Geophys. Res. Lett.*, *24*, 2219–2222, doi:10.1029/97GL02101.

Allard, P., et al. (1991), Eruptive and diffuse emissions of CO_2 from Mt. Etna, *Nature*, *351*, 387–391, doi:10.1038/351387a0.

Allard, P., B. Behncke, S. D'Amico, M. Neri, and S. Gambino (2006), Mount Etna 1993–2005: Anatomy of an evolving eruptive cycle, *Earth Sci. Rev.*, *78*, 85–114, doi:10.1016/j.earscirev.2006.04.002.

Allen, A. G., C. Oppenheimer, M. Ferm, P. J. Baxter, L. A. Horrocks, B. Galle, A. J. S. McGonigle, and H. J. Duffell (2002), Primary sulfate aerosol and associated emissions from Masaya Volcano, Nicaragua, *J. Geophys. Res.*, *107*(D23), 4682, doi:10.1029/2002JD002120.

Allen, A. G., T. A. Mather, A. J. S. McGonigle, A. Aiuppa, P. Delmelle, B. Davison, N. Bobrowski, C. Oppenheimer, D. M. Pyle, and S. Inguaggiato (2006), Sources, size distribution, and downwind grounding of aerosols from Mount Etna, *J. Geophys. Res.*, *111*, D10302, doi:10.1029/2005JD006015.

Andronico, D., et al. (2005), A multi-disciplinary study of the 2002–03 Etna eruption: Insights into a complex plumbing system, *Bull. Volcanol.*, *67*, 314–330, doi:10.1007/s00445-004-0372-8.

Bagnato, E., A. Aiuppa, F. Parello, S. Calabrese, W. D'Alessandro, T. A. Mather, A. J. S. McGonigle, D. M. Pyle, and I. Wängberg (2007), Degassing of gaseous (elemental and reactive) and particulate mercury from Mount Etna volcano (southern Italy), *Atmos. Environ.*, *41*, 7377–7388, doi:10.1016/j.atmosenv.2007.05.060.

Bobrowski, N., R. von Glasow, A. Aiuppa, S. Inguaggiato, I. Louban, O. W. Ibrahim, and U. Platt (2007), Reactive halogen chemistry in volcanic plumes, *J. Geophys. Res.*, *112*, D06311, doi:10.1029/2006JD007206.

Caltabiano, T., R. Romano, and G. Budetta (1994), SO_2 flux measurements at Mount Etna (Sicily), *J. Geophys. Res.*, *99*(D6), 12,809–12,819, doi:10.1029/94JD00224.

Cohn, C. A., S. Mueller, E. Wimmer, N. Leifer, S. Greenbaum, D. R. Strongin, and M. A. A. Schoonen (2006), Pyrite-induced hydroxyl radical formation and its effect on nucleic acids, *Geochem. Trans.*, *7*(3), 11 pp., doi:10.1186/1467-4866-7-3.

Delmelle, P., J. Stix, P. J. Baxter, J. Garcia-Alvarez, and J. Barquero (2002), Atmospheric dispersion, environmental effects and potential health hazard associated with the low-altitude gas plume of Masaya volcano, Nicaragua, *Bull. Volcanol.*, *64*, 423–434, doi:10.1007/s00445-002-0221-6.

Delmelle, P., M. Lambert, Y. Dufrene, P. Gerin, and N. Óskarsson (2007), Gas/aerosol-ash interaction in volcanic plumes: New insights from surface analysis of fine volcanic ash, *Earth Planet. Sci. Lett.*, *259*, 159–170, doi:10.1016/j.epsl.2007.04.052.

Gaudichet, A., M. De Anglais, R. Lefevre, J. R. Petit, Y. S. Korotkevitch, and V. N. Petrov (1988), Mineralogy of Insoluble Particles in Vostok Antarctic Ice Core Over the Last Climatic Cycle (150 kyr), *Geophys. Res. Lett.*, *15*(13), 1471–1474, doi:10.1029/GL015i013p01471.

Gauthier, P. J., and M. F. Le Cloarec (1998), Variability of alkali and heavy metal fluxes released by Mt. Etna volcano, Sicily, between 1991 and 1995, *J. Volcanol. Geotherm. Res.*, *81*, 311–326, doi:10.1016/S0377-0273(98)00002-X.

Giggenbach, W. F. (1987), Redox processes governing the chemistry of fumarolic gas discharges from White Island, New Zealand, *Appl. Geochem.*, *2*, 143–161, doi:10.1016/0883-2927(87)90030-8.

Gislason, S. R., and E. H. Oelkers (2003), Mechanism, rates, and consequences of basaltic glass dissolution: II. An experimental study of the dissolution rates of basaltic glass as a function of pH and temperature, *Geochim. Cosmochim. Acta*, *67*, 3817–3832, doi:10.1016/S0016-7037(03)00176-5.

Halmer, M. M., H. U. Schminke, and H. F. Graf (2002), The annual volcanic gas input into the atmosphere, in particular into the stratosphere: A global data set for the past 100 years, *J. Volcanol. Geotherm. Res.*, *115*, 511–528, doi:10.1016/S0377-0273(01)00318-3.

Han, Z. J., and L. Holappa (2001), Formation of metal droplets from gas bubbles bursting on iron melt, *Steel Res.*, *72*, 434–438.

Han, Z. J., and L. Holappa (2003), Bubble bursting phenomenon in gas/metal/slag systems, *Metall. Mater. Trans. B*, *34*, 525–532, doi:10.1007/s11663-003-0020-2.

Hinds, W. C. (1999), *Aerosol Technology: Properties, Behavior, and Measurement of Airborne Particles*, 483 pp., John Wiley, New York.

Horwell, C. J., and P. J. Baxter (2006), The respiratory health hazards of volcanic ash: A review for volcanic risk mitigation, *Bull. Volcanol.*, *69*, 1–24, doi:10.1007/s00445-006-0052-y.

Lefevre, R., A. Gaudichet, and M. A. Billongalland (1986), Silicate microspherules intercepted in the plume of Etna volcano, *Nature*, *322*, 817–820, doi:10.1038/322817a0.

Martin, R. S., T. A. Mather, and D. M. Pyle (2006), High-temperature mixtures of magmatic and atmospheric gases, *Geochem. Geophys. Geosyst.*, *7*, Q04006, doi:10.1029/2005GC001186.

Mather, T. A., A. G. Allen, C. Oppenheimer, D. M. Pyle, and A. J. S. McGonigle (2003a), Size-resolved characterisation of soluble ions in the particles in the tropospheric plume of Masaya volcano, Nicaragua: Origins and plume processing, *J. Atmos. Chem.*, *46*, 207–237, doi:10.1023/A:1026327502060.

Mather, T. A., D. M. Pyle, and C. Oppenheimer (2003b), Tropospheric volcanic aerosol, in *Volcanism and the Earth's Atmosphere*, *Geophys. Monogr. Ser.*, vol. 139, edited by A. Robock, and C. Oppenheimer, pp. 189–212, AGU, Washington, D. C.

Mather, T. A., A. G. Allen, B. M. Davison, D. M. Pyle, C. Oppenheimer, and A. J. S. McGonigle (2004a), Nitric acid from volcanoes, *Earth Planet. Sci. Lett.*, *218*, 17–30, doi:10.1016/S0012-821X(03)00640-X.

Mather, T. A., C. Oppenheimer, A. G. Allen, and A. J. S. McGonigle (2004b), Aerosol chemistry of emissions from three contrasting volcanoes in Italy, *Atmos. Environ.*, *38*, 5637–5649, doi:10.1016/j.atmosenv.2004.06.017.

Mather, T. A., J. R. McCabe, V. K. Rai, M. H. Thiemens, D. M. Pyle, T. H. E. Heaton, H. J. Sloane, and G. R. Fern (2006), Oxygen and sulfur isotopic composition of volcanic sulfate aerosol at the point of emission, *J. Geophys. Res.*, *111*, D18205, doi:10.1029/2005JD006584.

Matsumoto, A., and T. K. Hinkley (2001), Trace metal suites in Antarctic pre-industrial ice are consistent with emissions from quiescent degassing of volcanoes worldwide, *Earth Planet. Sci. Lett.*, *186*, 33–43, doi:10.1016/S0012-821X(01)00228-X.

Maynard, A. D. (1995), The development of a new thermophoretic precipitator for scanning-transmission electron-microscope analysis of ultrafine aerosol-particles, *Aerosol Sci. Technol.*, *23*, 521–533, doi:10.1080/02786829508965334.

Meeker, G. P., and T. K. Hinkley (1993), The structure and composition of microspheres from the Kilauea volcano, Hawaii, *Am. Mineral.*, *78*, 873–876.

Moune, S., F. Faure, P.-J. Gauthier, and K. W. W. Sims (2007), Pele's hairs and tears: Natural probe of volcanic plume, *J. Volcanol. Geotherm. Res.*, *164*, 244–253, doi:10.1016/j.jvolgeores.2007.05.007.

Naughton, J. J., A. A. Lewis, D. Hammond, and D. Nishimoto (1974), The chemistry of sublimates collected directly from lava fountains at Kilauea volcano, Hawaii, *Geochim. Cosmochim. Acta*, *38*, 1679–1690, doi:10.1016/0016-7037(74)90185-9.

Óskarsson, N. (1981), The chemistry of Icelandic lava incrustations and the latest stages of degassing, *J. Volcanol. Geotherm. Res.*, *10*, 93–111, doi:10.1016/0377-0273(81)90057-3.

Pirrie, D., A. R. Butcher, M. R. Power, P. Gottlieb, and G. L. Miller (2004), Rapid quantitative mineral and phase analysis using automated scanning electron microscopy (QemSCAN); potential applications in forensic geoscience, *Geol. Soc. Spec. Publ.*, *232*, 123–136.

Rose, W. I., R. L. Chuan, W. F. Giggenbach, P. R. Kyle, and R. B. Symonds (1986), Rate of sulfur dioxide and particle emission from White Island Volcano, New Zealand and an estimate of the total flux of major gaseous species, *Bull. Volcanol.*, *48*, 181–187, doi:10.1007/BF01087672.

Russell, L. M., and E. G. Singh (2006), Submicron salt particle production in bubble bursting, *Aerosol Sci. Technol.*, *40*, 664–671, doi:10.1080/02786820600793951.

Spadaro, F. R., R. A. Lefevre, and P. Ausset (2002), Experimental rapid alteration of basaltic glass: Implications for the origins of atmospheric particulates, *Geology*, *30*, 671–674, doi:10.1130/0091-7613(2002)030<0671:ERAOBG>2.0.CO;2.

Symonds, R. B., W. I. Rose, and M. H. Reed (1988), Contribution of Cl-bearing and F-bearing gases to the atmosphere by volcanos, *Nature*, *334*, 415–418, doi:10.1038/334415a0.

Toutain, J. P., J. P. Quisefit, P. Briole, P. Aloupogiannis, P. Blanc, and G. Robaye (1995), Mineralogy and chemistry of solid aerosols emitted from Mount Etna, *Geochem. J.*, *29*, 163–173.

Varekamp, J. C., E. Thomas, M. Germani, and P. R. Buseck (1986), Particle geochemistry of volcanic plumes of Etna and Mount St-Helens, *J. Geophys. Res.*, *91*(B12), 12,233–12,248, doi:10.1029/JB091iB12p12233.

Vogt, R., P. J. Crutzen, and R. Sander (1996), A mechanism for halogen release from sea-salt aerosol in the remote marine boundary layer, *Nature*, *383*, 327–330, doi:10.1038/383327a0.

Watson, I. M., and C. Oppenheimer (2000), Particle size distributions of Mount Etna's aerosol plume constrained by Sun photometry, *J. Geophys. Res.*, *105*(D8), 9823–9829, doi:10.1029/2000JD900042.

Watson, I. M., and C. Oppenheimer (2001), Photometric observations of Mt. Etna's different aerosol plumes, *Atmos. Environ.*, *35*, 3561–3572, doi:10.1016/S1352-2310(01)00075-9.

A. Aiuppa, CFTA, Università degli Studi di Palermo, Via Archirafi 36, Palermo, I-90123, Italy.

A. G. Allen, Analytical Chemistry Department, Chemistry Institute, Sao Paulo State University, 14800-900 Araraquara, SP, Brazil.

C. J. Horwell, Institute of Hazard and Risk Research and Department of Earth Sciences, Durham University, South Road, Durham DH1 3LE, UK.

R. S. Martin, Department of Earth Sciences, University of Cambridge, Downing Street, Cambridge CB2 3EQ, UK. (rsm45@cam.ac.uk)

T. A. Mather and D. M. Pyle, Department of Earth Sciences, University of Oxford, Parks Road, Oxford OX1 3PR, UK.

M. Power, Intellection U. K. Ltd., North Wales Business Park, Abergele, Conwy LL22 8LJ, UK.

E. P. W. Ward, Department of Materials Science and Metallurgy, University of Cambridge, Pembroke Street, Cambridge CB2 3QZ, UK.